Journal of

Applied and Computational Mechanics

Shahid Chamran
University of Ahvaz

Research Paper

Generation of a Quadrilateral Mesh based on NURBS for Gyroids of Variable Thickness and Porosity

Mariana S. Flores-Jimenez[1] , Arturo Delgado-Gutiérrez[2] , Rita Q. Fuentes-Aguilar[1] , Diego Cardenas[1]

[1] School of Engineering and Sciences, Tecnológico de Monterrey. Av. General Ramón Corona 2514, Col. Nuevo México, Zapopan, Jalisco, México, CP 45138

[2] School of Engineering and Sciences, Tecnológico de Monterrey. Calle del Puente 222, Col. Ejidos de Huipulco, Tlalpan, Ciudad de México, México, CP 14380

Abstract. The Gyroid is a periodic minimal surface explored in different applications, such as architecture and nanotechnology. The general topology is suitable for the construction of porous structures. This paper presents a non-iterative, novel methodology for the generation of a NURBS-based Gyroid volume. The Gyroid fundamental patch is defined with the Weierstrass parameterization. Furthermore, the geometry is manipulated to generate a structured mesh, allowing better element quality for FEM and IGA simulations. The re-parametrization is carried out by a Least-Squares approximation with a parametric NURBS surface, enabling a better definition of the mid-surface normals for the generation of the complete Gyroid volume. Different cases of variational thickness and porosity are presented to validate the versatility of our method.

Keywords: Gyroid, NURBS, Parametric mesh, Triply periodic minimal surfaces (TPMS).

1. Introduction

Triply periodic minimal surfaces (TPMS) are surfaces with local minimal area and no self-intersections. They are symmetric and periodic in three independent directions, having zero mean curvature (H) and negative Gaussian curvature (K), separating space into equal volume domains [1]. The most studied are the Diamond (D), the Primitive (P), and the Gyroid (G), and they are topologically equivalent with genus 3, related by a Bonnet transformation, which is a rotation around the tangent plane, where each point on the surface preserves its normal vector. Additionally, TPMS can be deformed, generating surfaces with Constant Mean Curvature (CMC). The CMC can be formed by minimizing the area that encloses a volume not equal to 50%. Another type of deformation is the "parallel surface", which shifts at a constant distance along the normal surface [2].

Due to these properties, TPMS have been proposed and tested in different areas. For instance, they are becoming popular in the field of architecture and mechanics, mainly because the weight and amount of material can be reduced. Their possibilities include tension-active roof structures, glass walls, bridges, and high-rise buildings [3]. In [4], the authors proposed that TPMS can be used in the aerospace industry as protective and damper layers. TPMS have also been explored for distillation membranes, where they showed a significant advantage over commercial membranes for water flux and heat transfer [5], this potential arises from their intrinsic vibratory properties and their capacity to be varied in terms of elasticity, damping, the volume ratio of interconnected porosity and permeability. In this sense, the Gyroid has proved to be lighter and stronger than other cell structures, because it is a bi-continuous isotropic structure [6]. It has been also used in the nanotechnology field, for example, in the design of a supercapacitor [7], where a double-gyroid vanadium network was implemented, and the highly ordered structure showed a high specific capacitance. It has been studied for new configurations of graphene, to create a strong block, yet lighter than air [8].

Additionally, the Gyroid has been identified in nature, like in biological membranes and bio-photonic structures, therefore, in the tissue engineering field, it has been used to design scaffolds, being recognized as one of the most promising geometries to enhance bone growth [9]. It is reported that Gyroid bone scaffolds fabricated by selective laser sintering, showed that the concave shape of the wall of the pores, helped cell migration and blood vessels formation [10]. Moreover, cell proliferation in this scaffold type, incremented in comparison with rectangular and square geometries, due to a 10-times greater permeability [11].

As can be noticed, TPMS, particularly the Gyroid, has a lot of potential applications in different fields, therefore, their design and simulation should be more explored with the goal of making it easier, faster, and more accurate. However, their realization as a 3D volume has not been an easy task, due to their mathematical complexity, which has hindered a wider adaptation of TPMS in different 3D models. That is why TPMS have been approximated in an implicit way with nodal equations, where the quality of the approximation depends on the number of terms in the Fourier series. Nevertheless, the surfaces obtained with the implicit method are neither minimal nor CMC surfaces, thus removing their properties of H=0 and K<0 that make them ideal for multiple applications [2]. This can be more noticeable in the tissue engineering field, where the change in the scaffold curvature can substantially affect the fate of the seeded cells, for example by compressing their nucleus [12].

In addition, one of the main problems of using the implicit approach is that the quality of the mesh is not suitable for numerical analysis. Typically, the required mesh for structural analysis must avoid highly skewed elements and a large aspect ratio to minimize the numerical error in the computation of the gradient and the stiffness matrix. It is also necessary to go through a process of triangulation, to obtain the mesh and to be able to render the figure. This can be costly in terms of time and computational memory, and the control of intersections between triangles can be complicated.

Nevertheless, there are several examples in the literature of the use of the implicit equation to model TPMS. In [13], the authors generated a TPMS unit cell with the implicit equation using the software *K3dSurf*. The object was then imported to a Computer-Aided Design (CAD) environment using the mesh as building blocks and finally intersected with another shape by Boolean operations. A similar methodology was taken in [14], where a Gyroid was constructed using scalar fields, taking as positive, the values outside the contour, and as negatives, the ones inside, while values exactly on the surface were zero. The porosity was controlled by changing the period of the implicit equation, achieving different surfaces with a constant porosity in the range from 2% to 98%, this does not mean a gradient in the same scaffold, but different separated designs, then, a solid model was generated and intersected with a Computational Tomography (CT) image.

Another example is presented in [15], where they also used the level set approach to creating the *MSLattice* software, which allows the control of TPMS topology, the relative density, cell size, and hybridization between lattices, however, the authors stated that the software is limited to not be able to lattice an arbitrary CAD shape for the purpose of light-weighting. Among the investigations that are based on the design of hybrid or heterogeneous scaffolds, in [16] it is presented a scaffold for a femoral condyle bone, based on points obtained from a CT scan, which were combined with a geometry made with different TPMS substructures, that were joined using the sigmoid function. On another hand, the authors in [17], designed a heterogeneous porous scaffold with a non-uniform threshold period, by combining implicit TPMS, marching cubes, and T-splines. One more option to handle the TPMS is with the *Surface Evolver* software [18]. It was created to represent surfaces described with a list of vertices. This list is used then to refine a triangular mesh using iteration algorithms, for example, the Newton-Raphson method, and certain constraints to reduce the energy of the surface in question, as a function of the position of each vertex.

It can be observed that all these studies have in common the use of the implicit equation and the need to use a triangulation method to obtain the mesh, also complicating the transition between different units, causing undesired bridges or deformations in the structure because of the use of sigmoid or step functions. In all cases, the original geometry is lost, along with its curvature properties. This problem is accompanied by the challenges in computer simulation related to the reaching of high accuracy in geometry representation and flow solution when the geometry is so complex, mostly with space-time computational methods [19]. This then leads to the search for new design and simulation strategies to be able to define exactly the TPMS, thus exploring the parametric approach and later using the re-parameterization with Non-Uniform Rational Basis Spline (NURBS).

NURBS have become very popular in the field of computational design and simulation since NURBS basis functions allow the exact representation of complex geometries. This advantage has been useful for Topology Optimization (TO), as described in [20], where the authors used NURBS to address the problem of controlling the minimum size of geometric features identified in a structure. The proposed method allowed for setting a combination of control points and degrees of the NURBS blending functions, satisfying the minimum member size, and achieving geometries with a smooth boundary. That procedure was also adapted for controlling the maximum size [21]. In the same sense, NURBS hyper-surfaces allow a straightforward CAD reconstruction without a need to define a filter zone, since NURBS continuous parameters (control points and weights) are the new design variables. Therefore, they have also been applied for stress based TO [22], design of lightweight lattice structures [23], and problems related to dynamics [24] and heat conduction [25], for instance in biomechanics applications since they allow the modeling of complex geometries such as bone and muscle intersections [26].

What is more, NURBS can also be used in metamodeling applications, to fit non-convex sets of target points, combining with genetic algorithms and nonlinear programming problems, as detailed in [27], [28]. NURBS are used for many advanced applications of Isogeometric Analysis (IGA), due to significant accuracy improvements over traditional linear Finite Element Method (FEM), but without the proportional increase in computational cost [29]. Within this context, IGA is a paradigm aiming to bridge the gap between classical FEM and CAD, providing a true design through the complete analysis process. In the traditional process, complex geometries are first modeled by means of CAD tools and then converted into a computational mesh needed for the numerical solution of the governing partial differential equations. This has been a bottleneck in performing simulations. It is observed that meshing accounts for 80% of total analysis time in FEM, and the obtained mesh is only an approximate representation of geometry, which results in an error. The use of NURBS basis functions ensures exact geometry representation in IGA. Additionally, IGA gives a better solution per degree of freedom than FEM, because it converges to a true solution since continuity across knots is provided by NURBS basis [30]. The advantages of using isogeometric approaches have also been demonstrated in multi-scale optimization strategies of variable stiffness composites, as in [31], where the authors used Basis Spline surfaces to represent the polar parameters fields. Since TPMS are used in different fields, the fact that they are defined by NURBS functions can help in TO according to the application, since the geometry can now be accurately simulated.

The main contribution of this paper is to propose a new methodology to model TPMS, specifically the Gyroid, based on a non-iterative process for the approximation of the volume with a tri-variate NURBS. First, the implicit approach is replaced by the Weierstrass parametric equation, to find a fundamental patch of the surface, and subsequently to build a mesh with B-splines and NURBS. With this approach, it is expected that it will be easier to manipulate and deform the Gyroid, in terms of porosity, thickness and surface-to-volume ratio, so that it can be used in different applications, as well as to facilitate its posterior characterization, using finite element techniques or even isogeometric analysis. Moreover, the possession of a parametric mesh in the first place, allows the exact definition of the Gyroid, therefore preserving its main characteristics, which can be also useful to obtain its CMC companions. The Weierstrass parameterization for TPMS has been used only to describe them for a 50% volume, but with the approach proposed in this work, it is demonstrated that a porosity gradient can be obtained using a parametric mesh. The Gyroid is described in this paper because it is the most common one in several applications, but since it is related to the P and D surfaces by the Bonnet transformation, this methodology can be equally applied for those geometries.

The paper is organized as follows. First, section 2 describes the process for construction of the TPMS Fundamental Patch (FP) based on the Weierstrass parameterization. Secondly, the FP is used to generate a Semi-Fundamental Patch (SFP) that is conformed by four FPs that are linearly transformed. Once the SFP is constructed in the physical space, a fitting process is used to approximate a NURBS surface, defining the SFP as the target geometry. It is worth noting that for a better quality of the mesh elements for further numerical analysis (FEM and/or Computational Fluid Dynamics CFD), the fitting process generates a NURBS surface with a rectangular grid on its bi-variate parametric space. The parametric NURBS surface is also used to compute the surface normal, which are useful when the surface is extruded to construct a volume. Furthermore, a Bounding Cell (BC) is then constructed, by replicating six times the SFP, where each copy is linearly transformed by pre-defined rules. Similarly, the BC is also replicated four times and linearly transformed to construct the final Cubic Cell (CC), which has a triple-periodic property. Finally, the re-parameterized NURBS Gyroid is then defined as a mid-surface, which is extruded in both normal directions to generate a volumetric Gyroid.
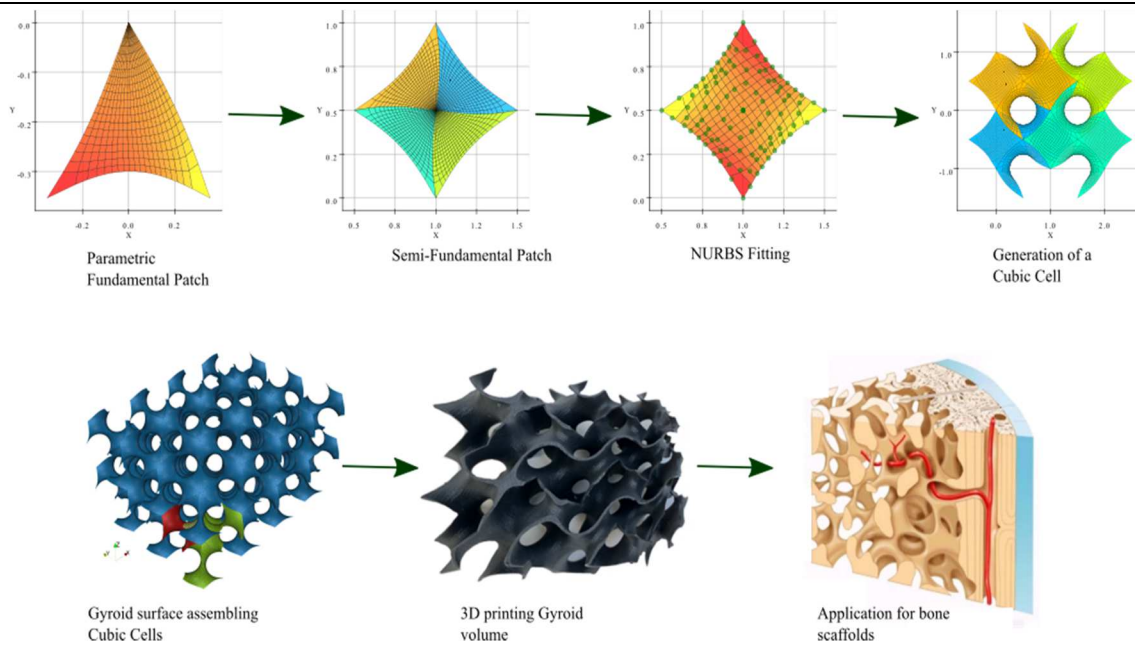
Fig. 1. Schematic representation of the followed methodology.

Subsequently, section 3 presents multiple cases to illustrate the capabilities of our novel method. First, a simple case with constant thickness, and porosity is conducted, where the mesh is proven to have excellent quality for numerical analysis. Secondly, multiple cases with variable thickness and/or porosity are carried out, showing the versatility of our model to generate complex topologies for specific cases. Additionally, a qualitative comparison is reported, where the numerical results and its 3D printed equivalent are shown side by side.

A schematic of the proposed design methodology is depicted in Fig. 1, where it is shown a summary of the followed process, starting with the generation of the FP and the subsequent NURBS fitting, ending with a Gyroid volume ready to be used in different applications, in this case, it is presented an example of a porous gradient volume to resemble bone porous anatomy. In this way, it is indicated that one of the main contributions of this paper is a process to design complex and intricate geometries with a controlled minimal curvature and a porosity gradient.

2. Methodology

In this section, the complete methodology for the generation of a NURBS volume, defined by the topological structure of a TPMS is presented. It is important to remark that the final parametric geometry can define variable thickness and porous size.

2.1 Weierstrass parametrization of the Gyroid fundamental patch

According to [32], a complete Gyroid can be described in terms of their fundamental patch (FP), since the entire surface is constructed using multiple copies of the FP, which are linearly transformed in order to modify their respective locations and orientations. For a proper definition of the FP, the Enneper-Weierstrass representation is used, which gives the coordinates of the FP, $\mathbf{F}$ ($\mathbf{F}_x$, $\mathbf{F}_y$, $\mathbf{F}_z$), in a physical space (x, y, z) in terms of the variables u and v, denoted in the complex plane as in eq. (1):

$$\mathbf{F}_x(u,v) = \frac{1}{2\sqrt{2}} \cdot \kappa \cdot e^{i\theta} \cdot \mathbb{R}\left(\text{ellipticF}\left[\arcsin\left(\frac{2\sqrt{2}(u+iv)}{(u+iv)^4 + 4(u+iv)^2 + 1} \right) \right], \frac{1}{4} \right),$$

$$\mathbf{F}_y(u,v) = -\frac{1}{2\sqrt{2}} \cdot \kappa \cdot e^{i\theta} \cdot \text{Im}\left(\text{ellipticF}\left[\arcsin\left(\frac{2\sqrt{2}(u+iv)}{(u+iv)^4 + 4(u+iv)^2 + 1} \right) \right], \frac{3}{4} \right), \qquad (1)$$

$$\mathbf{F}_z(u,v) = \frac{1}{4} \cdot \kappa \cdot e^{i\theta} \cdot \mathbb{R}\left(\text{ellipticF}\left[\arcsin\left(\frac{4(u+iv)^2}{\sqrt{(u+iv)^4 + 1}} \right) \right], 97 - 56\sqrt{3} \right),$$

where $\kappa = a\sqrt{K'' / KK''}$, $K = \text{ellipticK}(1/4)$, $K' = \text{ellipticK}(3/4)$, $K'' = K^2 + K'^2$, $\theta = \text{arccot}(K'/K) \approx 38.0147°$. In this nomenclature, ellipticF is the incomplete elliptic integral of the first kind and ellipticK is the complete elliptic integral of the first kind, while κ is the normalization factor, and a is the length of the bounding box, defined as 1 in order to have a unit cell, and θ is the angle related to the Bonnet transformation of the TPMS.

Figure 2 shows the complex domain where eq. (1) must be evaluated. Shaded area is the intersection of a circle of radius $\sqrt{2}$ centered at $(-\sqrt{2}/2, -i\sqrt{2}/2)$ and in the positive quadrant of the complex plane. The perimeter of the circle intersects the real and imaginary axis at $\sqrt{3} - 1/\sqrt{2}$ respectively. Parameters u and v are discretized using the arc-length of the circle and the distance to the origin, creating a poplar mesh depicted in Fig. 2b). The complex space shown in Fig. 2b) is evaluated in eq. (1) to obtain the coordinates of the FP in the physical space. Once the fundamental patch $\mathbf{F}$ is mapped in the physical space (see Fig. 3), the surface is ready to be replicated and linearly transformed for the construction of the semi-fundamental patch.
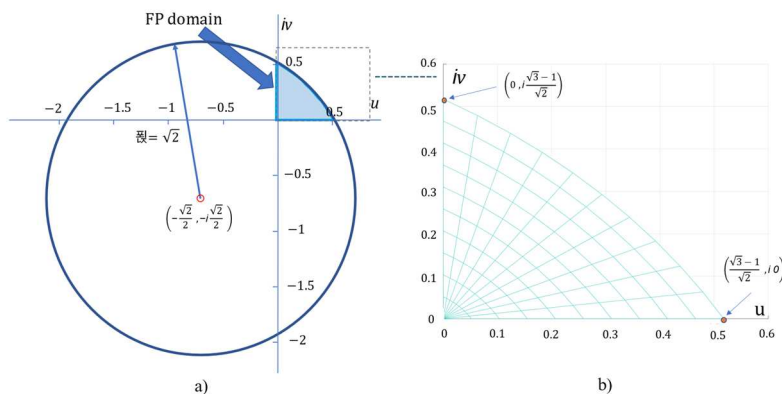
Fig. 2. Integration domain in the complex plane for the Gyroid based on [32]. a) Circle enclosing the domain. b) Specific arc of the integration domain.
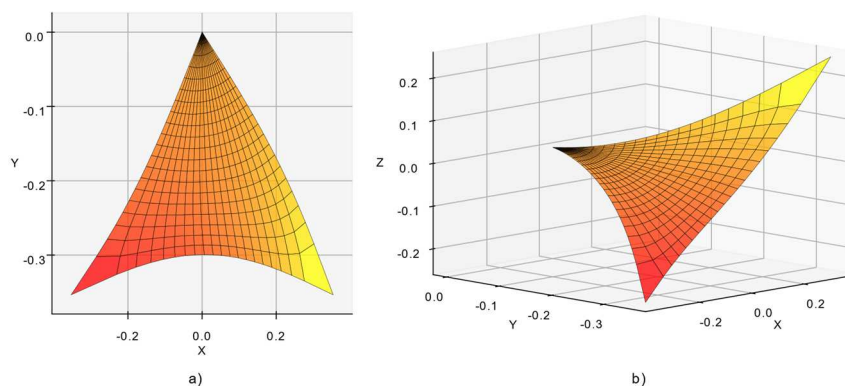

Fig. 3. Fundamental patch in the physical space (x, y, z). a) Top view in the x-y plane. b) Three-dimensional view.

2.2 Generation of the semi-fundamental patch

Following the work of Gandy *et al.* [32], the fundamental patch **F** (**F**$_x$, **F**$_y$, **F**$_z$) is defined as a fundamental unit of symmetry, from which the complete surface can be generated, applying the corresponding linear transformations. In his work, Gandy proposed to join twelve FPs to form the structure known as the *Bounding Cell* (BC). Furthermore, eight BC are then used to construct a final *Cubic Cell* (CC). Nevertheless, this work proposes a different approach to generate a proper mesh, to simplify the approximation process with NURBS surfaces.

First, four FPs are considered to construct a surface **S** denoted as the *Semi-Fundamental Patch* (SFP):

$$\mathbf{S} = \{\mathbf{F}_1 \mathbf{F}_2 \mathbf{F}_3 \mathbf{F}_4\} \tag{2}$$

The linear transformations considered in this work are rotations, translations, and reflections. The translation vector is defined in eq. (3):

$$\mathbf{A}(a_x, a_y, a_z) = \begin{bmatrix} a_x \\ a_y \\ a_z \end{bmatrix}, \tag{3}$$

where a_x, a_y and a_z are the constant offsets for each direction. Additionally, the rotation matrices are indicated in eq. (4):

$$\mathbf{R}_x(\varphi) = \begin{bmatrix} 1 & 0 & 0 \\ 0 & \cos(\varphi) & -\sin(\varphi) \\ 0 & \sin(\varphi) & \cos(\varphi) \end{bmatrix}, \quad \mathbf{R}_y(\varphi) = \begin{bmatrix} \cos(\varphi) & 0 & \sin(\varphi) \\ 0 & 1 & 0 \\ -\sin(\varphi) & 0 & \cos(\varphi) \end{bmatrix}, \quad \mathbf{R}_z(\varphi) = \begin{bmatrix} \cos(\varphi) & -\sin(\varphi) & 0 \\ \sin(\varphi) & \cos(\varphi) & 0 \\ 0 & 0 & 1 \end{bmatrix}, \tag{4}$$

where φ is the rotation angle. Similarly, to generate the corresponding reflections, the matrices in eq. (5) are used:

$$\mathbf{T}_x = \begin{bmatrix} -1 & 0 & 0 \\ 0 & 1 & 0 \\ 0 & 0 & 1 \end{bmatrix}, \quad \mathbf{T}_y = \begin{bmatrix} 1 & 0 & 0 \\ 0 & -1 & 0 \\ 0 & 0 & 1 \end{bmatrix}, \quad \mathbf{T}_z = \begin{bmatrix} 1 & 0 & 0 \\ 0 & 1 & 0 \\ 0 & 0 & -1 \end{bmatrix}, \tag{5}$$

To construct the complete SFP **S**, the linear transformations in eq. (6), are applied to **F** on the physical space (x, y, z):

$$\begin{aligned}
\mathbf{F}_1 &= \mathbf{T}_{yz} \mathbf{R}_z(-\pi/4) \mathbf{F} + \mathbf{A}(1, 1/2, 1/4), \\
\mathbf{F}_2 &= \mathbf{T}_x \mathbf{R}_z(+\pi/4) \mathbf{F} + \mathbf{A}(1, 1/2, 1/4), \\
\mathbf{F}_3 &= \mathbf{T}_{xz} \mathbf{R}_z(-\pi/4) \mathbf{F} + \mathbf{A}(1, 1/2, 1/4), \\
\mathbf{F}_4 &= \mathbf{T}_y \mathbf{R}_z(+\pi/4) \mathbf{F} + \mathbf{A}(1, 1/2, 1/4),
\end{aligned} \tag{6}$$

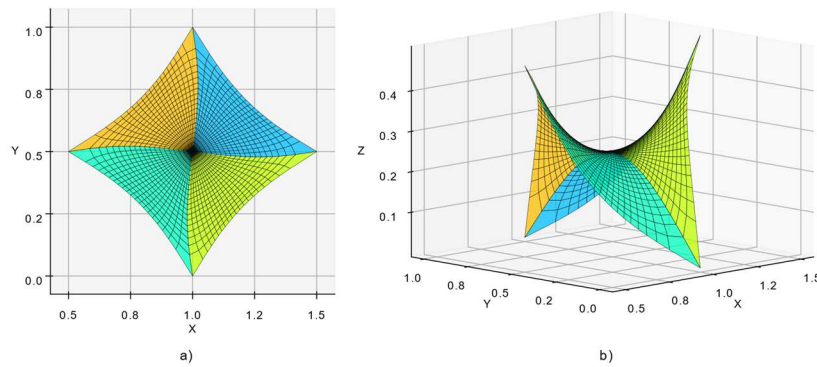where $\mathbf{T}_{yz} = \mathbf{T}_z \mathbf{T}_y$ and $\mathbf{T}_{xz} = \mathbf{T}_z \mathbf{T}_x$.

Fig. 4. Semi-Fundamental patch in the physical space (x, y, z). a) Top view in the x-y plane. b) Three-dimensional view.

In Fig. 4 the complete SFP is shown. It is worth noting that the SFP is mapped in parametric space with a polar coordinate system. This configuration can be problematic when the geometry is intended for simulations discretized for Finite Element Method (FEM) or Iso-geometric Analysis (IGA). For this, it is desirable to create a re-parameterization where the quality of the elements (especially closer to the center of the patch) is acceptable. Such re-parameterization can be developed if the SFP is approximated by a NURBS surface, which is the approach followed in this work.

2.3 NURBS approximation for the semi-fundamental patch

One of the most versatile technologies used in Computer Aided Design (CAD) are the Non-uniform Rational Basis Splines (NURBS) functions. These functions have excellent properties for the definition of complex curves, surfaces, and volumes. Additionally, NURBS geometries are appropriate for defining smooth patches that can be attached together to form complex assemblies, such as the TPMS.

First, a B-spline basis function is typically defined as $N_{i,p}(\xi)$, where p is the order of degree of the basis function, i is the ith basis function and ξ is the parametric coordinate. Furthermore, the set of B-splines basis functions are constructed using a knot vector $\bar{\xi}$, that is composed by knots (ξ_i) which are non-decreasing numbers, as indicated in eq. (7):

$$N_{i,0}(\xi) = \begin{cases} 1 & \text{if } \xi_i \le \xi \le \xi_{i+1}, \\ 0 & \text{otherwise.} \end{cases}$$

$$N_{i,p}(\xi) = \frac{\xi - \xi_i}{\xi_{i+p} - \xi_i} N_{i,p-1}(\xi) + \frac{\xi_{i+p+1} - \xi}{\xi_{i+p+1} - \xi_{i+1}} N_{i+1,p-1}(\xi). \tag{7}$$

To define the general description of the B-splines, NURBS shape functions are defined as in eq. (8):

$$R_{i,p}(\xi) = \frac{N_{i,p}(\xi) w_i}{\sum_{i=0}^{n} N_{i,p}(\xi) w_i} \tag{8}$$

where w_i are the weights for each B-spline function [33]. These weights affect the contribution of each control point in the shape of the curve. If a parametric surface is defined by a set of bi-variate NURBS shape functions, the set can be constructed by using two uni-variate shape functions (one for each parametric coordinate), as indicated in eq. (9):

$$R_{i,j}(\xi, \eta) = \frac{N_{i,p}(\xi) M_{j,q}(\xi) w_{i,j}}{\sum_{k=0}^{n} \sum_{l=0}^{m} N_{k,p}(\xi) M_{l,q}(\xi) w_{k,l}} \tag{9}$$

In this way, a NURBS surface is generated by simply multiplying each shape function with its respective control point, as in eq. (10):

$$\mathbf{S}(\xi, \eta) = \sum_{i=0}^{n} \sum_{j=0}^{m} R_{i,j}(\xi, \eta) \mathbf{P}_{i,j} \tag{10}$$

where $\mathbf{P}$ is the unknown set of control points.

Fitting a cloud of points with a NURBS surface is often formulated as an unconstrained nonlinear problem [34]. To find a better approximation for the surface, there are several design parameters to be tuned, such as weights, knot-vectors, degrees of the basis functions, and a number of control points. One of the most advanced strategies to deal with this type of problem is proposed by [35, 36], where the authors developed a general hybrid optimization algorithm, allowing the simultaneous variation of the number and values of the design parameters. Once the NURBS system is defined, the coordinates of the control points can be achieved by simply solving the linear system of eq. (11):

$$\mathbf{R}\mathbf{P} = \mathbf{S} \tag{11}$$

A NURBS surface can be approximated by using a method known as the Least Squares Minimization [37]. First, both sides of eq. (11) are multiplied by $\mathbf{R}^T$, as indicated in eq. (12):

$$(\mathbf{R}^T \mathbf{R})\mathbf{P} = \mathbf{R}^T \mathbf{S} \tag{12}$$

It is worth noting that this operation creates an invertible matrix $\mathbf{R}^T \mathbf{R}$, allowing to find the control points with eq. (13):

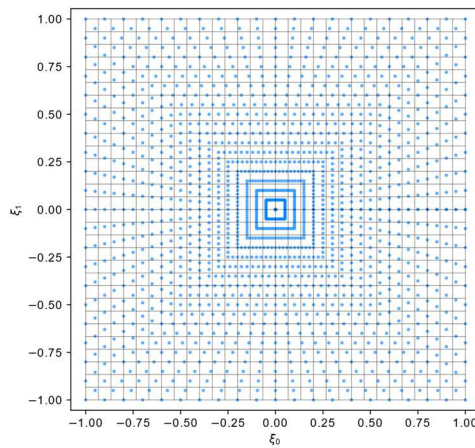$$\mathbf{P} = (\mathbf{R}^T \mathbf{R})^{-1} \mathbf{R}^T \mathbf{S} \tag{13}$$

Fig. 5. Cloud points of the SFP mapped in the parametric space $\xi(\xi_0, \xi_1)$.
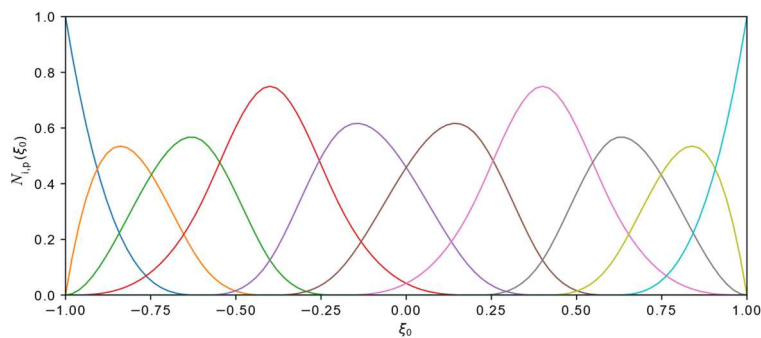

Fig. 6. Uni-variate shape functions for $N_{i,p}(\xi)$.

Furthermore, the approximation can be achieved even if the cloud points are unsorted. The only requirement needed is to carefully associate the locations of the points in the parametric space. By having described the definition of a NURBS surface, and the procedure to approximate the surface with a known set of cloud points, this work generates the control points needed to construct a NURBS-based SFP. It is worth noting that the NURBS parameter's configuration has been selected with a trial-and-error process since an optimization process to find the best NURBS parameters is out of the scope of this work.

As mentioned before, it is necessary to map the known cloud point of the SFP into the 2D parametric space. For this, the following procedure is used. First, consider a parametric space $\xi(\xi_0, \xi_1)$, ranging from -1 to 1 in both coordinates as shown in Fig. 5, this allows to relate of the center of the NURBS surface with the center of the SFP. By inspecting the distribution of the SFP points in Fig. 4, it is necessary to have a similar distribution in the parametric space. For this, the next step is to define a linearly distributed radial path in all directions, ranging from the center to the borders of the parametric space. It is possible to distribute the radial path in a different manner, but for simplicity, this process is configured with the linear radial distribution. With this configuration, each point in the SFP (see Fig. 4a) is associated with a point located in the parametric space ξ (see Fig. 5), allowing the generation of a better quality mesh once the control points are obtained by using eq. (13).

In the present work, a cubic ($p = q = 3$) NURBS surface is considered. The shape functions degrees have been selected by exploring the behavior of the fitting process. This exploration shows that if the degrees are increased, the generated surface possesses some oscillations, similar to the interpolation of Lagrangian polynomial surfaces. On the other hand, if the degree is reduced, the first derivative can be limited to a linear function or even a constant. This derivative is relevant for the computation of normal vectors at any location, which is then used for the generation of a SFP volume with a specific width. By selecting the cubic NURBS surface, a second order derivative is acquired, and the oscillations of the fitting process have been reduced.

To find the least amount of control points needed to fit the surface properly, a trial-and-error process is used. By inspecting multiple scenarios, the number of control points for each parametric coordinate is set to 10, creating a control mesh of 10x10 points. The knot vector sequence for both parametric coordinates is the same, and is set as a non-uniform sequence in eq. (14):

$$\overline{\xi}_0 = \overline{\xi}_1 = [-1, -1, -1, -1, -0.6, -0.4, -0.2, 0.2, 0.4, 0.6, 1, 1, 1, 1] \tag{14}$$

With this configuration, the uni-variate shape functions for both $N_{i,p}(\xi)$ and $M_{j,q}(\eta)$ are identical, only $N_{i,p}(\xi)$ is shown in Fig. 6. The non-uniform property of the knot vector enables a parameter to improve the mesh distribution over all the parametric space. This configuration can be modified for specific purposes, depending on the problem that is intended to solve.

Furthermore, the weights of all control points $w_{i,j}$ are graphically described in Fig. 7. Specifically, the corner control points have been set with a weight of 0.25, allowing more contribution to the remaining control points. Additionally, the first and second rings of the control mesh have been set with weights of 0.75 and 1.5 respectively. The remaining control points have been set with a weight of 1.0. Once again, the weights configuration can be modified for different purposes.

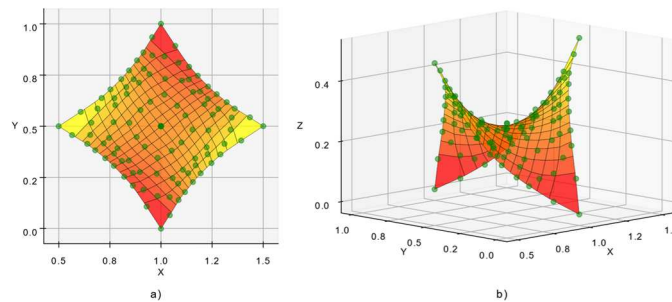**Fig. 7.** Weight configuration for the 10x10 control points.

Fig. 8. Approximated Semi-Fundamental Patch in the physical space (*x*, *y*, *z*). a) Top view in the *x*-*y* plane. b) Three-dimensional view.

By obtaining the NURBS surface control points with eq. (13), the SFP shown in polar coordinates in Fig. 4., is now approximated and constructed as a NURBS surface with a rectangular and regularized grid (see Fig. 8). Overall, the SFP quadrilateral mesh has a better element distribution, and the aspect ratio of the quadrilaterals is adequate for the FEM and IGA implementations. The node density at the center of the SFP is now well distributed, compared with the mesh reported in Fig. 3. Additionally, it has been proven that the reconstruction of the SFP can be achieved with a control mesh of 10x10 control points.

At this point in the methodology, it is safe to replace the original SFP with the approximated SFP for the reconstruction of the complete geometry.

2.4 Generation of the Bounding Cell using multiple Semi-Fundamental Patches

Similar to the generation of the SFP, a *Bounding Cell* (BC) can be constructed by a set of SFPs. In this work, the BC is reconstructed by using six SFPs that are recursively transformed. In other words, the first SFP will generate the second one, then, the second one will generate the third one and so on. First the BC **B** can be defined as the next expression:

$$\mathbf{B} = \{\mathbf{S}_1 \mathbf{S}_2 \mathbf{S}_3 \mathbf{S}_4 \mathbf{S}_5 \mathbf{S}_6\} \tag{15}$$

In eq. (15), $\mathbf{S}_1$ is the original SFP shown in Fig. 8. Subsequently the remaining five SFP from **B** can be computed as indicated in eq. (16):

$$\mathbf{S}_2 = \mathbf{D}\mathbf{S}_1 + \mathbf{A}(0,0,1),$$
$$\mathbf{S}_3 = \mathbf{D}\mathbf{S}_2 + \mathbf{A}(0,0,1),$$
$$\mathbf{S}_4 = \mathbf{D}\mathbf{S}_3 + \mathbf{A}(0,0,1), \tag{16}$$
$$\mathbf{S}_5 = \mathbf{D}\mathbf{S}_4 + \mathbf{A}(0,0,1),$$
$$\mathbf{S}_6 = \mathbf{D}\mathbf{S}_5 + \mathbf{A}(0,0,1),$$

where the transformation matrix **D** is denoted in eq. (17):

$$\mathbf{D} = \mathbf{T}_z \mathbf{R}_y(-\pi/2)\mathbf{R}_x(-\pi/2) \tag{17}$$

The resultant BC geometry **B** is shown in Fig. 9. It should be stressed out that the BC geometry has an excellent alignment, which proves that the SFP approximation process has been carried out correctly. Additionally, the quadrilateral aspect-ratio of the SFP is maintained in the complete BC geometry, since the linear transformation is not intended for deformation of the SFP.

2.5 Generation of the cubic cell by assembling four Bounding Cells

By following a similar procedure for the constructions of the SFP and the BC, the *Cubic-Cell* (CC) geometry is generated by assembling four BCs, which are also recursively transformed. For this part, three different sets of symmetry operations will be applied to the original coordinates of the bounding cell. In this work, the CC is denoted as:

$$\mathbf{C} = \{\mathbf{B}_1 \mathbf{B}_2 \mathbf{B}_3 \mathbf{B}_4\}, \tag{18}$$
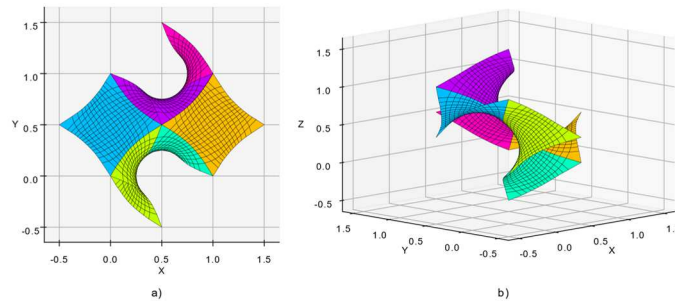
Fig. 9. Bounding Cell in the physical space (x, y, z). a) Top view in the x-y plane. b) Three-dimensional view.
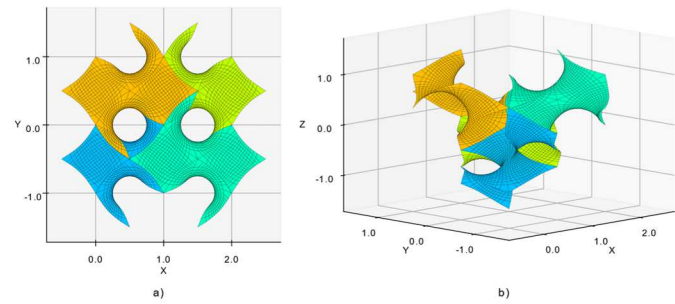

Fig. 10. Cubic Cell in the physical space (x, y, z). a) Top view in the x-y plane. b) Three-dimensional view.
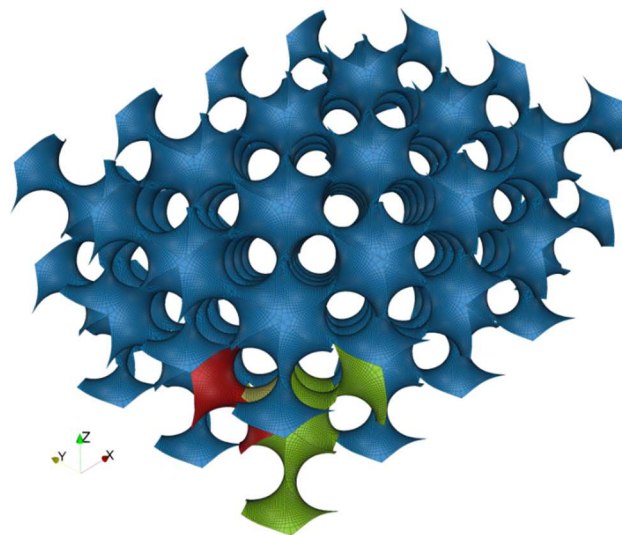

Fig. 11. Complete TPMS mesh in the physical space (x, y, z).

where the BCs are linearly transformed following eq. (19):

$$\begin{aligned}
\mathbf{B}_1 &= \mathbf{B}, \\
\mathbf{B}_2 &= \mathbf{T}_y \mathbf{B} + \mathbf{A}(1,0,1), \\
\mathbf{B}_3 &= \mathbf{T}_{yz} \mathbf{B} + \mathbf{A}(1,1,0), \\
\mathbf{B}_4 &= \mathbf{T}_{xy} \mathbf{B} + \mathbf{A}(1,0,-1).
\end{aligned} \tag{19}$$

In Fig. 10, the complete CC is shown, where the transformed bounding cells are highlighted with different colors. This geometry is the main unit that can be periodically replicated to construct the complete TPMS.

2.6 Periodical repetition of the cubic cell to generate the complete Gyroid surface

In this work, the complete TPMS is generated by repeating the *Cubic-Cell* multiple times in each direction. Additionally, only translations (no reflections or rotations) are required. As an example, the TPMS is conformed with four CCs in the X-direction, three in the Y-direction, and two in the Z-direction. For visualization purposes, the complete TPMS mesh is presented in Fig. 11, differentiating the SFP in yellow, the BC in red, and the CC in green. It has been proven that the alignment of the CCs is successfully achieved, and the complete mesh has excellent quality for the quadrilateral elements.

At this point, the complete mesh has a total of 230,400 quadrilateral elements. However, this mesh is only constructed as a reference mid surface for a complex three-dimensional volume. The next step is to generate a complete Gyroid volume by using the referenced surface and the computation of its respective normal components.
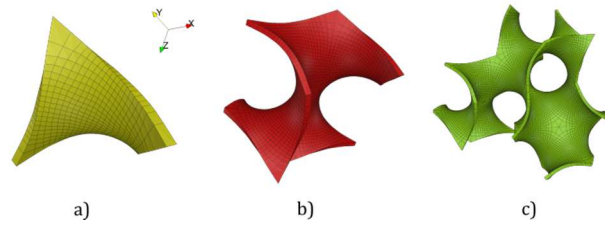
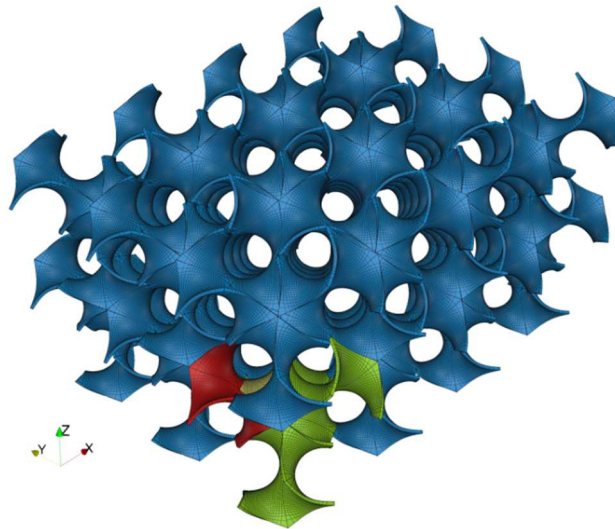**Fig. 12.** Volumetric patches in the physical space (x, y, z). a) SFP, b) BC, c) CC.

Fig. 13. Complete gyroid volume in the physical space (x, y, z).

2.7 Computation of NURBS-TPMS normals

Previously, the SFP was approximated with a three-dimensional NURBS surface. This allows the complete knowledge of the geometry, which enables the computation of its spatial derivatives. The surface differentiation is useful in this work, since the normal vectors of a surface can be simply defined by the cross product of the surface partial derivatives on each parametric direction, as indicated in eq. (20):

$$\mathbf{n}\left(\xi_0,\xi_1\right) = \frac{\partial \mathbf{S}}{\partial \xi_0} \times \frac{\partial \mathbf{S}}{\partial \xi_1} = \mathbf{S}_{\xi_0} \times \mathbf{S}_{\xi_1},$$

$$\widehat{\mathbf{n}} = \frac{\mathbf{n}}{|\mathbf{n}|}.$$

(20)

By defining the normal vectors of the parametric surface, it is now possible to extrude the mid-TPMS to create a 3D volume. For the computation of the partial derivatives, NURBS surface derivatives for each direction are described in eq. (21):

$$\mathbf{S}_{\xi_0} = \frac{\partial \mathbf{R}_{i,p}\left(\xi_0,\xi_1\right)}{\partial \xi_0}\mathbf{P} = \mathbf{R}_{\xi_0}\mathbf{P},$$

$$\mathbf{S}_{\xi_1} = \frac{\partial \mathbf{R}_{i,p}\left(\xi_0,\xi_1\right)}{\partial \xi_1}\mathbf{P} = \mathbf{R}_{\xi_1}\mathbf{P},$$

(21)

where **P** are the control points obtained for the NURBS-SFP. With eq. (21), it is possible to obtain the normal vectors using eq. (20).

2.8 Generation of the complete Gyroid volume

The NURBS-SFP has been defined along with the parametric definition of the normal vectors. By using the same linear transformations, the normal components can be transferred to the BC, CC, and the complete TPMS. This enables the capability to extrude the complete mid-surface and create a thickness to generate a complete Gyroid volume **V**. For illustration purposes Fig. 12, shows all three geometries that create the complete volume. Fig. 12a) shows the SFP volume created with the extrusion of the SFP mid-surface. Similarly, both the BC and the CC are shown in Fig. 12b) and 12c). The patches have been correctly extruded since the normal vectors are fully defined.

Finally, the complete Gyroid volume is presented in Fig. 13, where the SFP, BC, and CC are highlighted with the same colors presented in Fig. 11. The complete mesh in this example is conformed by 230,400 hexahedral elements. Qualitatively speaking, the complete volumetric mesh seems to have an excellent quality for both FEM and IGA simulations.

3. Results

The parametrized geometry defined in the previous sections can be used to create a hexahedral mesh for numerical (FEM and IGA) analysis. Additionally, geometry can be used to manufacture biomedical structures, by 3D printing.
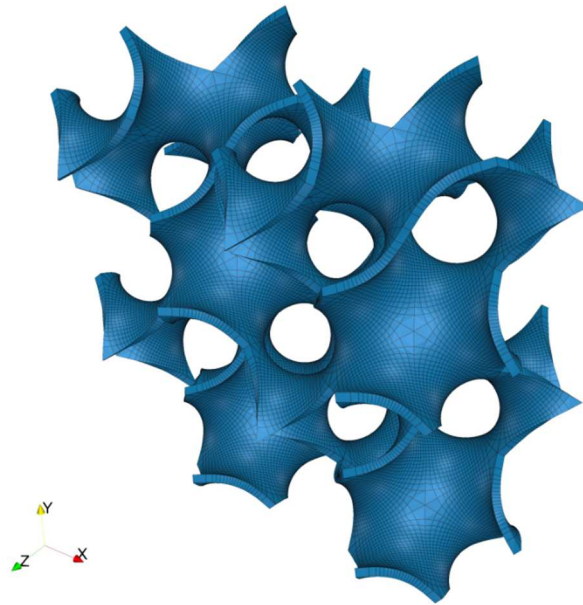
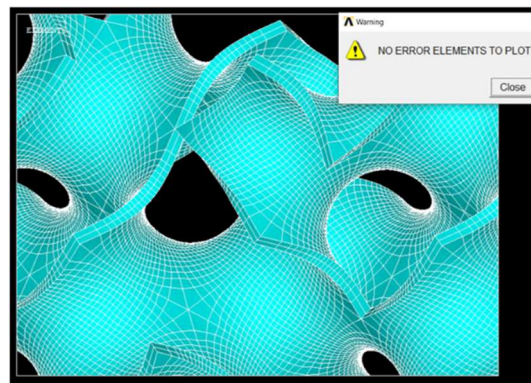**Fig. 14.** Computational mesh ready to import to FEM/CFD Software.

Fig. 15. ANSYS mesh reporting good quality solid mesh parameters for analysis.

3.1 3D Structural FEM mesh

Finite element analysis decomposes a 2D or 3D domain into a mesh, which is then used to solve a specific problem. It is well known that better results are obtained if a good quality of the structured mesh is achieved. Typically, errors in the stress gradient may be generated due to large element angles. On the other hand, small angles increase the condition of the stiffness matrix, degenerating the accuracy and the convergence of the solution [38]. The procedure proposed in this work can be used to generate a structured mesh for the volumetric gyroid. By evaluating the NURBS volume with a pre-specified resolution in the parametric space, a complete mesh of the gyroid can be generated, representing a reliable copy of the gyroid geometry, with suitable properties for FEM analysis. It is worth noting that an additional meshing step is no longer required.

Nowadays, most FEM software include a function for checking the quality of a mesh, prior to a specific analysis. To verify the quality of a mesh generated with the methodology described in this paper, a small portion of the gyroid volume shown in Fig. 14, is imported into ANSYS, by defining the mesh elements as linear hexahedrons. It is possible to observe in Fig. 15, the detail of the mesh in a portion of the total volume, showing that the mesh is completely structured, and the software does not detect any element with bad quality properties. The nodes and the connectivity of the mesh elements of Fig. 15 were created previously using the NURBS-based geometry of the Gyroid. By conducting this test, it is proven that the methodology presented in this paper allows the creation of structured high quality meshes to assure accurate FEM analysis results.

3.2 3D Printing

Since the complete Gyroid volume is represented parametrically, it is possible to define different shapes of the volume for specific purposes. As a qualitative result, this work presents the manufactured shape for three different cases:

1. Gyroid with thickness variable.
2. Gyroid with BC length variable.
3. Gyroid with thickness and BC length variable.

To manufacture the geometry, a 3D printing process was executed for all cases, with a *Form 2®* 3D printer from *Formlabs*. The first example is defined by the following properties:

Gyroid with thickness variable
Number of CC = n_x = 3, n_y = 3, n_z = 1.
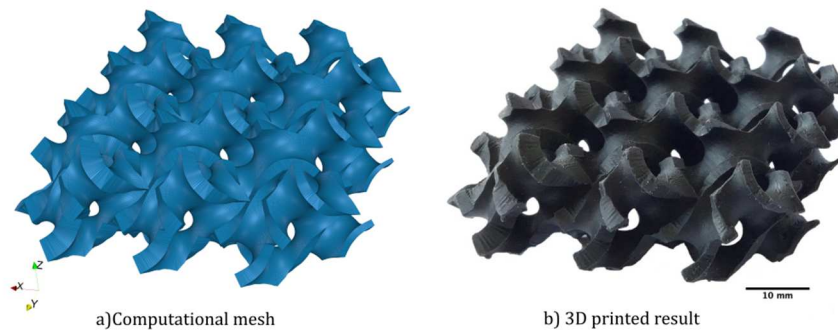Thickness factor = 0.08 + 0.05x + 0.02y.
BC length = 1.

Fig. 16. Gyroid with thickness variation in the *x* and *y* axis. a) Computational mesh, b) 3D printed Gyroid, with a size of
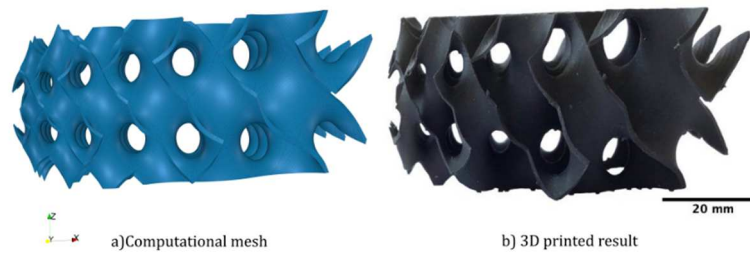*x* = 56.05 mm, *y* = 53.70 mm, *z* = 27.99 mm.

Fig. 17. Gyroid with BC length variation in the *x* and *y* axis. a) Computational mesh. b) 3D printed Gyroid, with a size of
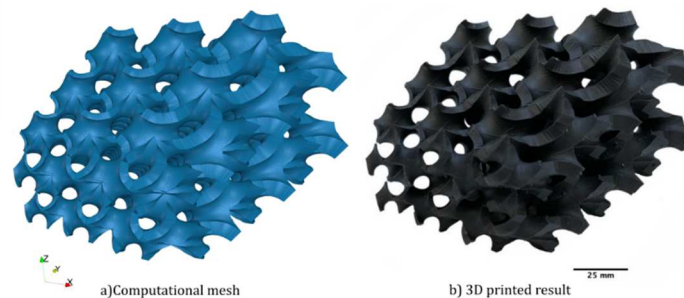*x* = 71.68 mm, *y* = 50.58 mm, *z* = 35.19 mm.

Fig. 18. Gyroid with thickness and BC length variation in the *x* and *y* axis. a) Computational mesh. b) 3D printed Gyroid, with a size of
x = 72.87 mm, *y* = 72.99 mm, *z* = 53.52 mm.

The printed geometry can be depicted in Fig.16b), while the computational mesh used to generate the geometry is presented in Fig. 16a). As shown in both figures, the thickness of the gyroid walls is decreasing linearly from left to right. This can be achieved since normal vectors of the Gyroid mid-surface are fully defined by the parametric description of the gyroid. Overall, the manufactured geometry is visually identical, proving that a gyroid with variable thickness can be used for further experimental analysis. Similarly, the second case has the following properties:

Gyroid with BC length variable
Number of CC = $n_x = 3$, $n_y = 3$, $n_z = 1$.
Thickness factor = 0.08.
BC length = $1 + 0.3x + 0.08y$.

Figure 17 also shows the comparison between the generated computational mesh for a variable bounding cell length. Once again, the resulting geometry was successfully manufactured through a 3D printing process. In this result, it is clearly visible the variation of the porous size, where the diameters are linearly increasing from left to right. This type of geometries can be used for specific biomedical studies, such as structural mechanics of bones.

Finally, the third case has the following properties:

Gyroid with thickness and BC length variable
Number of CC = $n_x = 3$, $n_y = 3$, $n_z = 2$.
Thickness factor = $0.08 + 0.05x + 0.02y$.
BC length = $1 + 0.05x + 0.08y$.

In the final case, both the thickness factor and the BC length have been set to increase linearly in the *x* and *y* directions. Figure 18a) shows the computational mesh, where the thickness of the walls is clearly increasing linearly from left to right. Additionally, the BC variable length generates a considerable transformation of the Gyroid. The resulting 3D printed geometry is shown in Fig. 18b), proving that the computational mesh has been successfully manufactured.

4. Discussions

The implicit approximation has been preferred over the Weierstrass parametric equation because in the parametric domain the structure could not be varied, that is, the Weierstrass equation only allowed a geometry that encloses 50% of the volume. Here it is demonstrated for the first time that a pore and thickness variation can be obtained using the parametric approach, because of the computation of the exact normal vectors in the NURBS-based semi fundamental patch, in this way preserving the exact zero mean curvature and negative gaussian, important for several applications.

Additionally, the design of a Gyroid based structure can be easy and straightforward in the sense that only a few inputs are needed, as shown in the examples on the 3D printing section, where only the desired number of Cubic Cells, the thickness factor, and the length of the Bounding Cell were set. This novel approach also allows the pore gradient with the smooth and continuous transition because no additional functions like a step or sigmoid are needed. In the future, this will also be useful for the hybridization of different TPMS.

In this work, the methodology was considered for the Gyroid, but its scope is not limited to this surface. Since the D and P surfaces are related to the Gyroid by the Bonnet transformation, the same process could be applied for them, only modifying the Fundamental Patch for each one by evaluating the Weierstrass equation in the corresponding integration domain, as indicated in [39], [40].

5. Conclusions

In this work, the complete methodology for the generation of a NURBS-based gyroid volume is presented in detail, addressing two important concerns: the preservation of the geometrical characteristics of the Gyroid, as well as the generation of a quality mesh for subsequent analysis like FEM and IGA.

First, a fundamental mid-surface patch generated with the Weierstrass parameterization is used to construct a semi fundamental mid-surface patch, by duplicating it and applying new linear transformations proposed in this work. The semi fundamental patch is basically the angular stone for the generation of the complete gyroid. Since the Weierstrass parameterization (used for the generation of the fundamental patch) is not suitable for the generation of good quality quadrilateral elements (non-skewed), the patch is re-parameterized. This is achieved by assigning each surface point a specific coordinate in a cartesian grid. By considering the semi fundamental mid-surface patch as a cloud of points, an approximation process for unsorted points is conducted to construct a parametric and NURBS-based patch. For future work, the fitting process can be implemented using an optimization process like the ones described in [35, 36], using the presented process as the "black box" of the algorithm. This will generate a better-fitted SFP.

The mid-surface semi fundamental patch is then extruded to generate a NURBS solid version. This is achieved by the complete definition of the NURBS parametric surface, which is capable to compute the surface normals at any location. Furthermore, the parametric surface also allows the generation of more complex Gyroid-like geometries since the thickness and porosity can be defined as variables along a specific direction. By duplicating the semi fundamental solid patch and applying additional linear transformations, the construction of an abounding cell and a cubic cell is conducted in the proposed process. The cubic cell solid is finally periodically repeated to generate the complete gyroid geometry.

To verify the quality and versatility of the generated geometry, two tests have been conducted in this work. First, the mesh generated is imported to ANSYS, which delivers a satisfactory result, indicating no elements with bad quality parameters. Secondly, the geometry is also used to physically construct a gyroid volume through a 3D printing process. Three cases with different parameters have been conducted, showing that the proposed methodology can construct complex geometries ready to manufacture.

The process presented in this work is designed for the generation of complex geometries that can be used for numerous areas of engineering. As an example, the organic-like properties of the Gyroid topology are suitable for biomedical applications. Additionally, aerospace applications can also take advantage of these topologies since the structural properties allow lighter components with excellent mechanical resilience and toughness. The novel and non-iterative methodology presented in this paper is explained in detail so that they can be coded by the reader.

Author Contributions

M.S. Flores-Jimenez initiated the project, presented the methodology, and conducted the simulations and experiments; A. Delgado-Gutierrez conducted simulation and analyzed the results and the methodology; R.Q. Fuentes-Aguilar examined the theory validation and the simulations; D. Cardenas developed the mathematical modeling and advised the work. The manuscript was written through the contribution of all authors. All authors discussed the results, reviewed, and approved the final version of the manuscript.

Acknowledgments

Conflict of Interest

The authors declared no potential conflicts of interest with respect to the research, authorship, and publication of this article.

Funding

Data Availability Statements

The datasets generated and/or analyzed during the current study are available from the corresponding author on reasonable request.
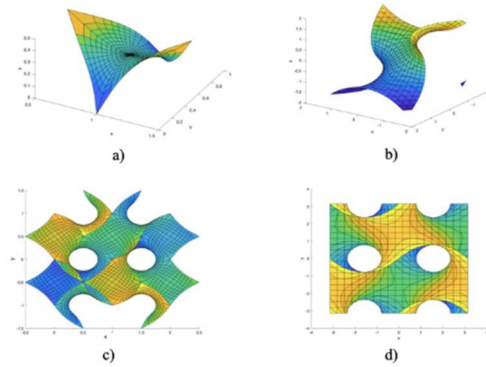
Fig. 19. Differences between the parametric and implicit Gyroid surface. a) Semi-fundamental patch obtained with the parametric approach. b) Segment of the implicit Gyroid (from $-\pi/2$ to $\pi/2$). c) Cubic Cell mesh after the re-parametrization with NURBS. d) Cubic Cell obtained with the implicit approach (from $-\pi$ to π).

Nomenclature

K	Gaussian curvature		φ	Rotation angle
H	Mean curvature		**F**	Fundamental Patch (FP)
κ	Normalization factor		**S**	Semi-Fundamental Patch (SFP), set of four FP
θ	Angle related to Bonnet transformation		**n**	Set of NURBS-TPMS normals
u	Real component of a complex number		**B**	Bounding Cell (BC), set of six SFP
v	Imaginary component of a complex number		**C**	Cubic Cell (CC), set of four BC
$\mathbb{R}$	Real part of a complex number		**D**	Transformation matrix
Im	Imaginary part of a complex number		**A**	Translation vector
$\mathbf{T}_x, \mathbf{T}_y, \mathbf{T}_z$	Reflection matrices		$\mathbf{R}_x(\varphi), \mathbf{R}_y(\varphi), \mathbf{R}_z(\varphi)$	Rotation matrices
$N_{i,p}(\xi)$	B-spline basis function		p	Order of degree of the basis function
ξ	Parametric coordinate		$\overline{\xi}$	Knot vector
$R_{i,p}(\xi)$	NURBS shape function		$R_{i,j}(\xi,\eta)$	Bi-variate NURBS shape function
$\mathbf{S}(\xi,\eta)$	NURBS surface		**P**	Set of control points

Acronyms

BC	Bounding Cell
CAD	Computer-Aided Design
CC	Cubic Cell
CFD	Computational Fluid Dynamics
FEM	Finite Element Method
FP	Fundamental Patch
IGA	Isogeometric Analysis
NURBS	Non-Uniform Rational Basis Spline
SFP	Semi-Fundamental Patch
TO	Topology Optimization
TPMS	Triply Periodic Minimal Surface

Appendix

Elliptic integrals

The incomplete elliptic integral of the first kind (ellipticF or F), can be defined as in eq. (22):

$$F(\varphi,k) = \int_0^{\varphi} \frac{d\theta}{\sqrt{1-k^2\sin^2\theta}}, \tag{22}$$

where φ refers to the amplitude of the function and is in the range $0 \leq \varphi \leq \pi/2$, while k is the modulus, which is a real number $0 < k < 1$, and θ is the modular angle or angular eccentricity [41]. According to eq. (1), for the fundamental patch, the first argument, φ, is the result of the arcsine function applied to a complex number, and k is a rational number different for each coordinate in the physical space. For its part, the complete integral of the first kind (ellipticK or K) can be defined as in eq. (23):

$$K(k) = \int_0^{\pi/2} \frac{d\theta}{\sqrt{1-k^2\sin^2\theta}}, \tag{23}$$

which is related to the incomplete integral of the first kind as: $K(k) = F(\pi/2, k)$ [41].

Curvature

In Fig. 19, it is shown a comparison between the surfaces obtained with the implicit and parametric approach. The mean curvature (H) was computed in MATLAB ® for the parametric one, and in *Surface Evolver* for the implicit one. In Fig. 19a), the Semi Fundamental patch of the Gyroid is depicted, and as expected, the H resulted in 0. On the other hand, it was difficult to obtain a patch with the implicit approach, therefore, to obtain one section of the complete Gyroid, the interval was set from $-\pi/2$ to $\pi/2$, as shown in Fig. 19b). The H resulted in 4.07^{-6}. The H was also computed for the complete Cubic Cell of the parametric Gyroid, which is shown in Fig. 17c). The mesh in this case was obtained after the NURBS re-parameterization, obtaining also 0, proving that the zero mean curvature is preserved even after the rotation and translation of the SFP. For its part, the H obtained in the implicit mesh for the cubic cell, shown in Fig. 19d), resulted in 3.3021^{-6}. With this short analysis, it can also be observed that the parametric Gyroid can be easier to handle, without showing abrupt interruptions in its shape, as shown in Fig. 19b).

References

[1] Karcher, H., Polthier, K., Construction of Triply Periodic Minimal Surfaces, *Philosophical Transactions: Mathematical, Physical and Engineering Sciences,* 354(1715), 1996, 2077-2104.
[2] Han, L., Che, S., An Overview of Materials with Triply Periodic Minimal Surfaces and Related Geometry: From Biological Structures to Self-Assembled Systems, *Advanced Materials,* 30(17), 2018, 1705708.
[3] Emmer, M., Minimal Surfaces and Architecture: New Forms, *Nexus Network Journal,* 15(2), 2013, 227-239.
[4] Sychov, M.M., Lebedev, L.A., Dyachenko, S.V., Nefedova, L.A., Mechanical properties of energy-absorbing structures with triply periodic minimal surface topology, *Acta Astronautica,* 150, 2018, 81-84.
[5] Thomas, N., Sreedhar, N., Al-Ketan, O., Rowshan, R., Al-Rub, R.K., Arafat, H., 3D printed triply periodic minimal surfaces as spacers for enhanced heat and mass transfer in membrane distillation, *Desalination,* 443, 2018, 256-271.
[6] Park, J.H., Lee, J.C., Unusually high ratio of shear modulus to Young's modulus in a nano-structured gyroid metamaterial, *Scientific Reports,* 7(10533), 2017.
[7] Wei, D., Scherer, M.R., Bower, C., Andrew, P., Ryhanen, T., Steiner, U., A nanostructured electrochromic supercapacitor, *Nano Letters,* 12(4), 2012, 1857-62.
[8] Qin, Z., Jung, G.S., Kang, M.J., Buehler, M.J., The mechanics and design of a lightweight three-dimensional graphene assembly, *Science Advances,* 3(1), 2017, 1601536.
[9] Yang, Y., Wang, G., Liang, H., Gao, C., Peng, S., Shen, L., Shuai, C., Additive manufacturing of bone scaffolds, *International Journal of Bioprinting,* 5(1), 2019, 148.
[10] Bobber, F.S.L, Zadpoor, A.A., Effects of bone substitute architecture and surface properties on cell response, angiogenesis, and structure of new bone, *Journal of Materials Chemistry B,* 5(31), 2017, 6175-6192.
[11] Melchels, F.P.W., Bertoldi, K., Gabbrielli, R., Velders, A.H., Feijen, J., Grijpma, D.W., Mathematically defined tissue engineering scaffold architectures prepared by stereolithography, *Biomaterials,* 31(27), 2010, 6909-6916.
[12] Callens, S.J.P, Uyttendaele, R.J.C, Fratila-Apachitei, L.E., Zadpoor, A.A., Substrate curvature as a cue to guide spatiotemporal cell and tissue organization, *Biomaterials,* 23, 2020, 119739.
[13] Fantini, M., Curto, M., Crescenzio, F., TPMS for interactive modelling of trabecular scaffolds for Bone Tissue Engineering, *Advances on Mechanics, Design Engineering and Manufacturing,* Springer, 2016.
[14] Walker, J.M., Bodamer, E., Kleinfehn, A., Luo, Y., Becker, M., Dean, D., Design and mechanical characterization of solid and highly porous 3D printed poly(propylene fumarate) scaffolds, *Progress in Additive Manufacturing,* 2, 2017, 99-108.
[15] Al-Ketan, O., Al-Rub, R.K.A., MSLattice: A free software for generating uniform and graded lattices based on triply periodic minimal surfaces, *Material Design & Processing Communications,* 2020, e205.
[16] Shi, J., Yang, J., Zhu, L., Li, L., Li, Z., Wang, X., A Porous Scaffold Design Method for Bone Tissue Engineering Using Triply Periodic Minimal Surfaces, *IEEE Access,* 6, 2018, 1015-1022.
[17] Feng, J., Fu, J., Shang, C., Lin, Z., Li, B., Porous scaffold design by solid T-splines and triply periodic minimal surfaces, *Computer Methods in Applied Mechanics and Engineering,* 336, 2018, 333-352.
[18] Brakke, K., The Surface Evolver and the Stability of Liquid Surfaces, *Philosophical Transactions of the Royal Society A: Mathematical, Physical and Engineering Sciences,* 354(1715), 1996, 2143-2157.
[19] Otoguro, Y., Mochizuki, H., Takizawa, K., Tezduyar, T.E., Space–Time Variational Multiscale Isogeometric Analysis of a tsunami-shelter vertical-axis wind turbine, *Computational Mechanics,* 66(6), 2020, 1443-1460.
[20] Costa, G., Montemurro, M., Pailhès, J., Minimum length scale control in a NURBS-based SIMP method, *Computer Methods in Applied Mechanics and Engineering,* 354, 2019, 963-989.
[21] Costa, G., Montemurro, M., Pailhès, J., Perry, N., Maximum length scale requirement in a topology optimization method based on NURBS hyper-surfaces. *CIRP Annals Manufacturing Technology,* 68, 2019, 153-156.
[22] Roiné, T., Montemurro, M., Pailhès, J., Stress-based topology optimization through non-uniform rational basis spline hyper-surfaces, *Mechanics of Advanced Materials and Structures,* 2021, 1-29.
[23] Montemurro, M., Bertolino, G., Roiné, T., A general multi-scale topology optimisation method for lightweight lattice structures obtained through additive manufacturing technology, *Composite Structures,* 258, 2021, 113360.
[24] Montemurro, M., Costa, G., Eigen-frequencies and harmonic responses in topology optimization: A CAD-compatible algorithm, *Engineering Structures,* 214, 2020, 110602.
[25] Montemurro, M., Refai, K., A Topology Optimization Method Based on Non-Uniform Rational Basis Spline Hyper-Surfaces for Heat Conduction Problems, *Symmetry,* 13(5), 2021, 888.
[26] Leyendecker, S., Penner, J., Biomechanical simulations with dynamic muscle paths on NURBS surfaces, *PAAM,* 19(1), 2019, 201900230.
[27] Audoux, Y., Montemurro, M., Pailhès, J., Non-Uniform Rational Basis Spline hyper-surfaces for metamodelling, *Computer Methods in Applied Mechanics and Engineering,* 364(4), 2020, 112918.
[28] Audoux, Y., Montemurro, M., Pailhès, J., A Metamodel Based on Non-Uniform Rational Basis Spline Hyper-Surfaces for Optimisation of Composite Structures, *Composite Structures,* 247, 2020, 112439.
[29] Moutsanidis, G., Li, W., Bazilevs, Y., Reduced quadrature for FEM, IGA and meshfree methods, *Computer Methods in Applied Mechanics and Engineering,* 373, 2021, 113521.
[30] Voruganti, H.K., Gondeagaon, S., Comparative study of isogeometric analysis with finite element analysis, *Energy Procedia,* 2016, 8.
[31] Fiordilino, G.A., Izzi, M.I., Montemurro, M., A general isogeometric polar approach for the optimisation of variable stiffness composites: Application to eigenvalue buckling problems, *Mechanics of Materials,* 153, 2021, 103574.
[32] Gandy, P., Klinowski, J., Exact computation of the triply periodic G ('Gyroid') minimal surface, *Chemical Physics Letters,* 321(5-6), 2000, 363-371.
[33] Cottrell, J., Hughes, T., Bazilevs, Y., *Isogeometric Analysis. Toward Integration of CAD and FEA,* John Wiley & Sons Inc, United States, 2009.
[34] Floater, M., Parametrization and smooth approximation of surface triangulations, *Computer Aided Geometric Design,* 14(3), 1997, 231-250.
[35] Costa, G., Montemurro, M., Pailhès, J., A General Optimization Strategy for Curve Fitting in the Non-Uniform Rational Basis Spline Framework, *Journal of Optimization Theory and Applications,* 176, 2018, 225-251.
[36] Bertolino, G., Montemurro, M., Perry, N., Pourroy, F., An Efficient Hybrid Optimization Strategy for Surface Reconstruction, *Computer Graphics Forum,* 40(6), 2021, 215-241.
[37] Chen, X.D., Ma, W., Paul, J.C., Cubic B-spline curve approximation by curve unclamping, *Computer-Aided Design,* 42(6), 2010, 523-534.
[38] Vartziotis, D., Wipper, J., Papadrakakis, M., Improving mesh quality and finite element solution accuracy by GETMe smoothing in solving the Poisson equation, *Finite Elements in Analysis and Design,* 66, 2013, 36-52.
[39] Gandy, P., Cvijovic, D., Mackay, A., Klinowski, J., Exact computation of the triply periodic D ('diamond') minimal surface, *Chemical Physics Letters,* 314(5-6), 1999, 543-551.

[40] Gandy, P., Klinowski, J., Exact computation of the triply periodic Schwarz P minimal surface, *Chemical Physics Letters,* 322(6), 2000, 579-586.
[41] Cvijovic, D., Klinowski, J. The T and CLP families of triply periodic minimal surfaces. Part 1. Derivation of parametric equations, *Journal de Physique I.*, 1992, 137-147.

ORCID iD

Mariana S. Flores-Jimenez https://orcid.org/0000-0002-1392-7660
Arturo Delgado-Gutiérrez https://orcid.org/0000-0002-1171-1225
Rita Q. Fuentes-Aguilar https://orcid.org/0000-0003-2559-539X
Diego Cardenas https://orcid.org/0000-0002-0512-6839

Publisher's Note Shahid Chamran University of Ahvaz remains neutral with regard to jurisdictional claims in published maps and institutional affiliations.